

See discussions, stats, and author profiles for this publication at: <https://www.researchgate.net/publication/276268413>

Large-Scale Molecular Packing and Morphology Dependent High Performance Organic Field-Effect Transistor by Symmetrical Naphthalene-Diimide Appended with Methyl Cyclohexane

ARTICLE *in* THE JOURNAL OF PHYSICAL CHEMISTRY C · MAY 2015

Impact Factor: 4.77 · DOI: 10.1021/acs.jpcc.5b03743

CITATIONS

2

READS

71

3 AUTHORS:



Anamika Kalita

Indian Institute of Technology Guwahati

4 PUBLICATIONS 3 CITATIONS

[SEE PROFILE](#)



Nimmakayala VV Subbarao

Indian Institute of Technology Guwahati

10 PUBLICATIONS 9 CITATIONS

[SEE PROFILE](#)



Parameswar K Iyer

Indian Institute of Technology Guwahati

92 PUBLICATIONS 1,472 CITATIONS

[SEE PROFILE](#)

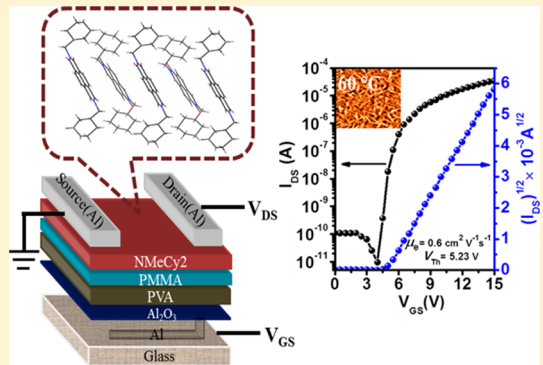
Large-Scale Molecular Packing and Morphology-Dependent High Performance Organic Field-Effect Transistor by Symmetrical Naphthalene Diimide Appended with Methyl Cyclohexane

Anamika Kalita,[†] Nimmakayala V. V. Subbarao,[†] and Parameswar K. Iyer*,^{†,‡}

[†]Centre for Nanotechnology and [‡]Department of Chemistry, Indian Institute of Technology Guwahati, Guwahati 781039, Assam, India

S Supporting Information

ABSTRACT: The influence of structural ordering of methyl cyclohexane appended naphthalene diimide (NMeCy₂) thin films and their correlation with enhanced device performances are presented here. The vacuum-deposited thin-film microstructure and morphology of NMeCy₂ have been investigated using thin-film X-ray diffraction (XRD), atomic force microscopy (AFM), and field emission scanning electron microscopy (FESEM) and were comparable with the bulk-phase crystalline structure and packing of NMeCy₂. The organic field-effect transistor (OFET) fabricated on a glass substrate consists of a bilayer polymer dielectric poly(methyl methacrylate) (PMMA) over poly(vinyl alcohol) (PVA) and an inorganic high-*k* dielectric Al₂O₃ as the third layer. NMeCy₂ thermally deposited at an optimized substrate temperature (*T*_{sub}) of 60 °C displayed excellent molecular packing over a large area that resulted in the improved field-effect performance with electron mobility (μ_e) value of 0.6 cm² V⁻¹ s⁻¹ and current on/off ratio ($I_{on/off}$) of 10⁶ via modifications in dielectric configuration. Furthermore, the device afforded an unprecedented threshold voltage (V_{Th}) of 5.23 V with this material. We have been successful in developing a facile, reliable, and cheap method to tune the dielectric features which can culminate in improved field-effect transport properties.



INTRODUCTION

Electronic devices based on small organic molecules and polymers have received considerable attention in recent years due to their low cost and milder operating conditions. Particularly, small molecule based organic semiconductors (OSCs) are versatile, inexpensive, reliable, easily functionalized, and used as active materials in organic light-emitting devices (OLEDs),¹ organic photovoltaics (OPVs),² and organic field-effect transistors (OFETs).³ The key problems of these molecules are the low mobility and low environmental stability. High mobility in OFETs is a prerequisite for fast response in high speed device applications. On the other hand, OFETs impose serious limitations to their practical applications due to the high operating voltage and high threshold voltage. Serious efforts have been devoted by researchers to improve these factors. This can be achieved by designing molecules with superior properties, device engineering, controlling the roughness and morphology of the dielectric, and OSC layers. The growth of OSCs and the alignment of crystalline layers on the dielectric surfaces are the key requirements for achieving high mobility.⁴ Generally, the hydrophobic surface is more favorable for the growth of OSCs than hydrophilic surfaces. Highly compact well-organized molecular packing among adjacent molecules with significant π -orbital overlap and the absence of grain boundaries facilitate efficient charge transport enabling

high mobility.⁵ The low operating voltage is one of the main criteria for the integrated digital circuits and biosensor applications. The reduction in the threshold voltage and operating voltage can be achieved by using high-*k* dielectrics or by decreasing the thickness of the dielectric by using a combination of high-*k*/low-*k* dielectric layers (d) ($C_i = \epsilon_0 k/d$).^{6,7} There are very few reports on low V_{Th} for *n*-channel OFETs with SiO₂ or polymer as dielectric. The V_{Th} is one of the most important device parameters in field-effect transistors, which is directly related to the charge trapping at the interface of organic-dielectric materials. In particular, control of V_{Th} is very crucial for constructing integrated transistor circuits because a shift of V_{Th} to a lower value results in a decrease in power consumption together with a high circuit operation speed.⁸

Among the small molecule *n*-type materials, naphthalene diimides are well studied for their applications in organic electronic devices. Shukla et al. reported a cyclohexyl-substituted NTCDI derivative that displayed μ_e of 6.2 cm² V⁻¹ s⁻¹ with $I_{on/off}$ and V_{Th} of 6×10^8 and ~58 V, respectively, on an OTS-modified SiO₂ substrate.⁹ This is the highest μ_e reported so far among the *n*-type OFETs due to the compact

Received: April 19, 2015

crystalline molecular packing in the thin-film phase.¹⁰ However, from the recent report by Mori's group the best values of μ_{e} , V_{Th} , and $I_{\text{on/off}}$ for the same material were found to be $0.52 \text{ cm}^2 \text{ V}^{-1} \text{ s}^{-1}$, 44 V, and 10^6 , respectively. It is relatively difficult to achieve lower V_{Th} with operating voltage below 100–120 V in this type of material as observed in this report.¹¹ It is well-known that high mobility can be obtained only in certain crystallographic planes and directions. Hence, it is important to correlate the transport behavior with the crystal structure and packing of the molecule and examine whether the thin-film deposition plane corresponds to the preferred plane for charge transport.¹² Apart from this it is well-known that, in a typical OFET, the first few layers of molecules at the dielectric–semiconductor interface are also responsible for charge transport.¹³

Herein, we report the synthesis of NMeCy2 and fabrication of *n*-channel OFETs using a stack of trilayer gate dielectric system ($\text{Al}_2\text{O}_3/\text{PVA}/\text{PMMA}$) to achieve high mobility and low operating voltage. Among high-*k* dielectrics, inorganic metal oxides are generally preferred. The reason for selecting an inorganic high-*k* Al_2O_3 dielectric layer is to provide high capacitance density and low leakage current. Among various polymer dielectric materials, PVA is highly versatile for OFETs due to its notable properties, viz., low leakage current, high dielectric constant, low temperature processing, good solubility in water, biocompatibility, low cost, and excellent film-forming abilities.^{14,15} It is widely recognized that PVA-like high-*k* materials are preferred as the gate dielectric due to their driving of high capacitance in OFET operation. However, under humid conditions, PVA-based OFETs exhibit pronounced hysteresis in transfer characteristics^{16–18} due to the charge traps at the semiconductor–dielectric interface due to the hydrophilic nature of PVA.¹⁹ Hysteresis-free OFETs can be made using PVA dielectrics without any cross-linkers or photosensitizers by applying a thin interface layer of hydrophobic/less polar PMMA that inhibits charge trapping activities²⁰ and enhances large-scale, well-organized closely packed crystalline grains. Finally we optimized the fabrication of OFETs using a suitable stack trilayer combination of dielectrics, and the factors such as μ_{e} , V_{Th} , operating voltage, and $I_{\text{on/off}}$ ratio could be improved under reliable, low cost processing conditions. Thus, a trilayer dielectric system is employed to construct OFETs with *n*-type material that showed high performances under vacuum.²¹

EXPERIMENTAL SECTION

Materials and Characterization. 1,4,5,8-Naphthalene dianhydride, cyclohexyl methaneamine, quinoline, zinc acetate, and PMMA (MW = 996 000 g/mol) were purchased from Sigma-Aldrich and were used without further purification. PVA (MW = 89 000–98 000 g/mol) was purchased from Alfa-Aesar. ^1H NMR and ^{13}C NMR were recorded on Bruker 600 MHz NMR spectrometers. UV-visible absorption spectra (both solution and thin film) were recorded on a PerkinElmer Lambda 35 spectrophotometer. Emission spectra (both solution and thin film) were measured on a Fluoromax-4 spectrophotometer. Electrochemical measurements were carried out using a CH instruments model 700D series Electrochemical workstation consisting of a three-electrode system, viz., Ag/AgNO_3 as the reference electrode, platinum wire as the counter electrode, and glassy carbon as the working electrodes. A 0.1 M tetra-*n*-butyl ammonium hexafluorophosphate (TBAP) in acetonitrile is used as a supporting electrolyte at a scan rate of 50 mV/s under an inert atmosphere.

Theoretical calculations were performed by the DFT method using the Gaussian 03 package with B3LYP hybrid functional and a 6-31G basis set. Thermogravimetric analysis (TGA) and differential scanning calorimetry (DSC) were performed on METTLER TOLEDO (model TG/SDTA 851 e and model DSC 1, Stare system) under N_2 flow at a heating rate of 10 °C/min. Thin-film XRD analysis was done by a RIGAKU TTRAX III diffractometer. A single-crystal structure was obtained using a Bruker Nonius SMART APEX CCD diffractometer equipped with a graphite monochromator and an Apex CCD camera. The diffraction data were collected at room temperature with Mo K α radiation ($\lambda = 0.71073 \text{ \AA}$). Structures were solved and refined by direct methods using SHELXS-97 and full-matrix least-squares on F2. AFM images were recorded on an Agilent 5500 AFM/SPM microscope. FESEM images were taken using the Sigma Carl ZEISS field emission scanning electron microscope.

Device Fabrication and Measurements. OFETs were fabricated using the bottom-gate, top-contact configuration. Herein, we utilized the low cost microscopic glass slides (roughness 1.8 nm) as the substrates for the fabrication of the devices on the $\text{Al}_2\text{O}_3/\text{PVA}/\text{PMMA}$ trilayer dielectric system. The glass substrates were cleaned in piranha solution (3:1 $\text{H}_2\text{SO}_4:\text{H}_2\text{O}_2$) and finally washed with deionized water several times. The cleaned substrates were dried under vacuum at 100 °C. A patterned 150 nm thick aluminum gate electrode was deposited using a thermal evaporator onto the glass substrates. The top surface was anodized to get 10 nm of Al_2O_3 to reduce the leakage current and increase the capacitance by decreasing the thickness of the subsequent polymer layers. Anodization was carried out with a constant current of $j = 0.6 \text{ mA cm}^{-2}$ driven through the electrolyte. A 0.001 M citric acid monohydrate ($\text{C}_6\text{H}_8\text{O}_7 \cdot \text{H}_2\text{O}$) was used to prepare electrolyte solution using ultrapure Milli-Q water. The aluminum-coated glass substrates were immersed into the electrolyte, which work as a working electrode (anode), and a platinum mesh served as the counter electrode (cathode). A Keithley 2400 source meter was used for supplying constant current. Constant current across the growing insulating Al_2O_3 layer was maintained by ramping up the voltage to a limiting anodization voltage (V_A), which was then maintained for several minutes until the current had completely decayed to below 5 μA . The thickness (d) of the resulting films can be controlled very precisely via the anodization voltage V_A with $d = cV_A$, where c is the “anodization ratio” value for aluminum (1.3 nm/V). The samples were subsequently rinsed in high-purity Milli-Q water heated at 60 °C to remove the citric acid molecules and carefully dried in a hot plate at a temperature of 100 °C. The bilayer polymeric dielectrics of PVA and PMMA were prepared by a spin-coating method. Initially, 3% PVA in water was spin coated at the rate of 3500 rpm for 60 s on an anodized alumina (Al_2O_3) surface, and the samples were dried in a vacuum oven for 60 min at 80 °C. A 1% PMMA solution in anisole was then spin coated above the dried PVA layer at the same rate for the same time and dried in a vacuum oven for 60 min at 80 °C. The total thickness of the dielectric layer was optimized to ~110 nm ($\text{Al}_2\text{O}_3(10 \text{ nm})/\text{PVA}(70 \text{ nm})/\text{PMMA}(30 \text{ nm})$) and measured using a profilometer (Dektat-150). The capacitance measurements on metal–insulator–metal (MIM) systems were carried out at 1 kHz–10 MHz at 30 mV modulation voltage with a Keithley 4200 SCS. A 60 nm thick film of NMeCy2 was deposited using thermal evaporation at a deposition rate of 0.4 Å/s under a base pressure of $5 \times 10^{-6} \text{ mbar}$. Aluminum source

and drain electrodes were deposited using thermal evaporation by using a shadow mask. The typical channel length (L) of the devices was 30 μm , and the channel width (W) was about 750 μm with width/length (W/L) as 25. The capacitance and electrical characteristics of OFET devices were carried out at room temperature in the dark under high vacuum using a Keithley 4200-SCS semiconductor parameter analyzer and a probe station (Lake Shore, $<1 \times 10^{-4}$ mbar) immediately after the devices were fabricated. The key device parameters such as μ_e , $I_{\text{on/off}}$, and V_{Th} were extracted from transfer characteristics, using the formula in the saturation regime

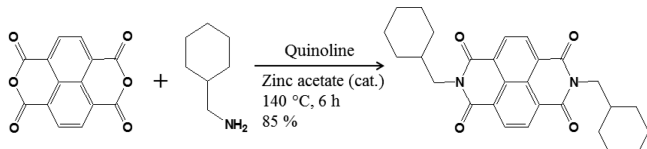
$$I_{\text{DS}} = (\mu_e WC_i / 2L)(V_{\text{GS}} - V_{\text{Th}})^2 \quad (1)$$

where C_i denotes the capacitance of the gate dielectric per unit area.

RESULTS AND DISCUSSION

Synthesis and Characterization. NMeCy2 was synthesized in high yields (85%) by a direct condensation method (Scheme 1). The detailed synthetic procedure and characterization are described in the Supporting Information (Figures S1 and S2).

Scheme 1. Synthetic Scheme of NMeCy2



Photophysical Properties. The absorption and emission properties of NMeCy2 were studied in both solution (DCM, 10^{-5} M) and thin-film (thickness 120 nm) phase (Figure 1a,b).

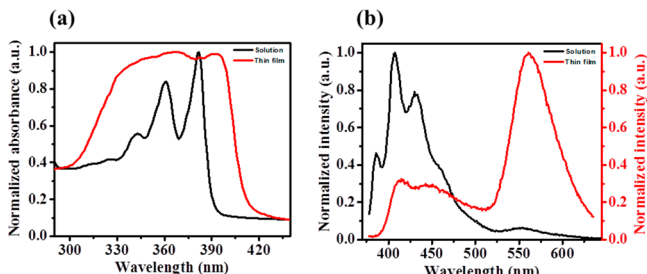


Figure 1. Normalized (a) absorption and (b) emission spectra of NMeCy2 in the solution and thin-film phase.

The absorption spectra of NMeCy2 in solution showed three characteristic peaks at 381, 360, and 341 nm corresponding to the 0–0, 0–1, and 0–2 vibronic transitions, respectively. However, the absorption peaks in thin film was broadened and red-shifted by 10 nm, attributed to the formation of J-aggregates.²² The optical band gap calculated using the absorption onset method was found to be 3.18 and 3.01 eV, respectively, for solution and thin-film phases. The emission spectra of NMeCy2 in solution exhibited three peaks at 385, 407, and 431 nm and a broad unstructured low intensity band appearing at 550 nm. The thin film exhibited a monomeric emission peak at 412 nm and a highly intense red-shifted emission peak at 560 nm confirming aggregation.

Electrochemical Properties. The electrochemical properties of NMeCy2 were investigated by cyclic voltammetry (CV) measurements to find the HOMO and LUMO positions of the molecule. A representative cyclic voltammogram for NMeCy2 is shown in Figure 2.

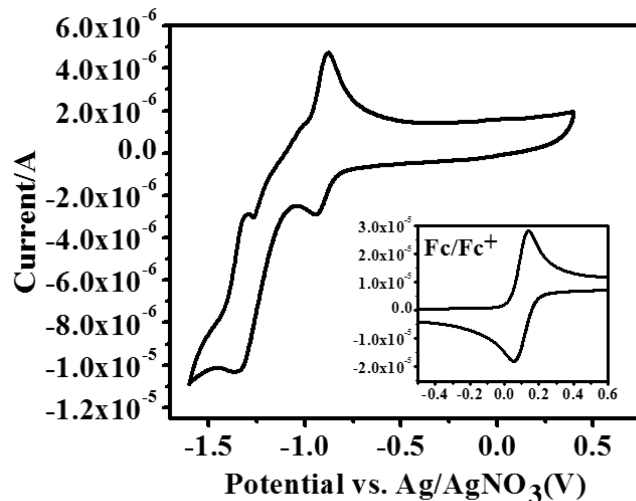


Figure 2. CV of the NMeCy2 molecule in acetonitrile. Inset: CV of the ferrocene used as reference.

The obtained electrochemical data are presented in Table 1. No oxidation waves could be observed up to 2 V. NMeCy2

Table 1. Half-Wave ($E_{1/2}$) Potentials, E_{HOMO} , E_{LUMO} , and Band Gap E_g of NMeCy2

reduction					
$E_{1/2}$ vs Ag/AgNO_3	$E_{2/1/2}$ vs Ag/AgNO_3	onset	E_{LUMO} (eV)	E_{HOMO} (eV)	E_g^{CV} (eV)
-0.94	-1.35	-1.32	-3.38	-6.383	3.00

exhibited two (quasi) reversible one-electron reduction waves corresponding to the formation of a radical anion and dianion. The LUMO energy level was estimated based on the following equation²³

$$\begin{aligned} E_{\text{LUMO}} \text{ (eV)} &= -(E_{\text{red-onset}} + 4.8) \\ &= -(E_{\text{pc-onset}} - E_{\text{Fc}} + 4.8) \end{aligned}$$

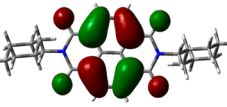
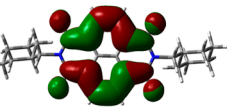
The HOMO level was calculated based on the optical band gap obtained from solid state absorption onset measurements.²⁴

$$\begin{aligned} E_{\text{LUMO}} &= -(4.8 + E_{\text{pc-onset}} - E_{\text{Fc}}) \\ &= -(-1.32 - 0.098 + 4.8) = -3.382 \text{ eV} \\ E_{\text{HOMO}} &= E_{\text{LUMO}} - E_g^{\text{optical}} = -3.382 - 3.01 \\ &= -6.383 \text{ eV} \\ (E_g^{\text{optical}} &= 1240/\lambda \text{ eV} = 1240/412 \text{ eV} = 3.01 \text{ eV}) \\ E_g &= E_{\text{LUMO}} - E_{\text{HOMO}} = 3.00 \text{ eV} \end{aligned}$$

Theoretical Calculations. DFT calculations using gas-phase geometry optimization reveal HOMO/LUMO values as -7.1287 eV/-3.5994 eV and an energy gap of 3.5 eV which are in good agreement with the experimental values. The HOMO

and LUMO orbitals and energy values are shown in Table 2. It was also observed that methyl cyclohexane groups do not

Table 2. HOMO/LUMO Energy Levels and Band Gap E_g^{Th} from DFT Calculation

HOMO	LUMO	E_g^{Th}
		3.5 eV

contribute to the frontier orbitals and are important only to attain the desired thin-film structure. The majority of the molecular orbital density was delocalized mainly on C atoms along the C–C bonds.

Thermal Studies. The thermal stabilities of NMeCy2 were determined using TGA and DSC techniques (Figure S3, Supporting Information). NMeCy2 exhibited excellent thermal stability with onset decomposition temperatures of around 305 °C under an inert gas environment. During DSC studies, a sharp transition at 334 °C was observed upon first heating that corresponds to melting of NMeCy2, while on second cooling the transition occurred at 288 °C. An evaporation temperature of NMeCy2 was optimized as 260 °C via TGA/DSC data using a ceramic crucible in high vacuum thermal evaporator. Thus, the thermal stability of the NMeCy2 is adequate for applications in optoelectronic devices.

Single-Crystal XRD and Pattern of Packing in the Solid State. The structural information on NMeCy2 was obtained by single-crystal X-ray analysis (Figure 3a,b).

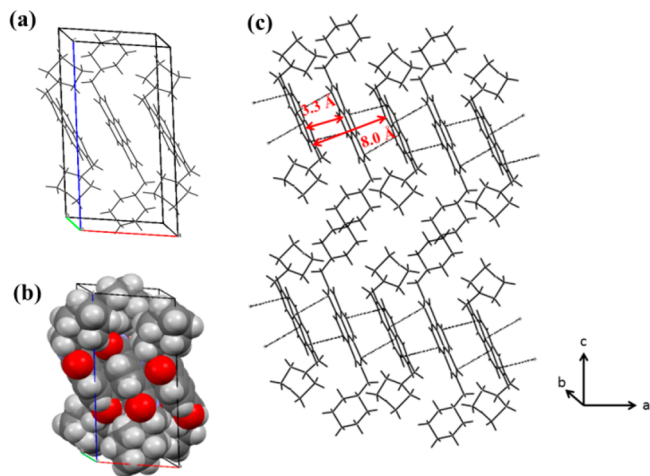


Figure 3. (a) Crystal structure of the unit cell, (b) space filling model, and (c) packing arrangement showing the shortest distance between two neighboring and two identical units in the crystal.

Crystallographic studies confirm the system as triclinic with P-1 space group ($a = 8.038(2)$ Å, $b = 8.7402(19)$ Å, $c = 17.845(4)$ Å, $\alpha = 100.535(9)$ °, $\beta = 97.165(9)$ °, $\gamma = 93.721(8)$ °, $Z = 1$), unlike monoclinic as reported for the cyclohexyl-substituted NTCDI molecule⁹ (Table S4, Supporting Information). The crystal packing structure of the molecule displayed a flip-flap stacking (Figure 3c) to minimize the steric hindrance between methyl cyclohexane side chains. It is evident that $\pi-\pi$

stacking between neighboring moieties was not completely cofacial but was slightly tilted with the shortest distance of around 3.3 Å. However, the distance between two similarly aligned molecules was observed to be ~8 Å. The observed intermolecular distance is comparable to the $\pi-\pi$ stacking distance commonly observed in cofacially packed linear acenes, i.e., 3.4–3.5 Å, which is required for strong electronic coupling and good charge mobility.²⁵ The energy minimization calculations on a stacked dimer at a fixed stacking distance of 3.3 Å give strong evidence for flip-flap intermolecular stacking that minimizes the steric hindrance between the methyl cyclohexane side chains. The total energy of the dimer decreases sharply upon rotating the molecules from zero degree and reaches the most stable stacking conformation at a rotation angle of 42.5° (Figure S5 and S6, Supporting Information). This dense packing facilitates the efficient charge transport in the crystals.

OFET Device Characteristics. To explore the semiconducting properties of NMeCy2 at different T_{sub} , OFET devices were fabricated with bottom-gate, top-contact configuration using trilayer gate dielectric materials. NMeCy2 used as the active layer was deposited by vacuum sublimation using a thermal evaporator. The schematic diagram of the device structure is illustrated in Figure 4, and the devices were tested under vacuum ($\sim 10^{-4}$ mbar) immediately after fabrication.

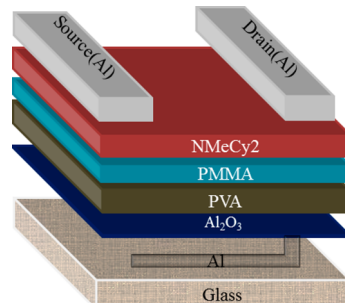


Figure 4. Schematic illustration of the OFET device fabricated on a trilayer dielectric system.

The OFET devices were fabricated by growing the organic semiconductor film at different $T_{\text{sub}} = \text{RT}, 60, 90,$ and 120 °C to monitor the effect and influence of T_{sub} on charge transport properties. Except the device set at $T_{\text{sub}} = 60$ °C, others displayed very poor μ_e value with relatively lower $I_{\text{on/off}}$ (Table S7, Supporting Information) confirming that T_{sub} is a key parameter in self-assembled growth of OSC layers at the dielectric–semiconductor interfaces which improves the charge carrier mobility and other OFET parameters. To arrive at some intricate correlation between device properties and its constituent layers, it is necessary to characterize each individual layer present in the device structure.

Thin-Film Morphology and Structural Characterization of Dielectric Layers and the Dielectric–NMeCy2 Interface at Different T_{sub} . The thin-film morphology and structural characterization of both dielectric materials and the dielectric–NMeCy2 interface is investigated by AFM, FESEM, and thin-film XRD analysis.

AFM Analysis. Generally, surface roughness of the gate dielectric is an important parameter that affects the device performance. Rough interfaces hinder the charge transport in the semiconductor by disturbing the morphology of the organic

semiconductor layer or by acting as physical traps. The typical surface morphology of the Al gate electrode, anodized Al_2O_3 , spin-coated PVA on anodized Al_2O_3 , and a thin layer of PMMA on $\text{Al}_2\text{O}_3/\text{PVA}$ dielectric (Figure 5) and organic semiconductor

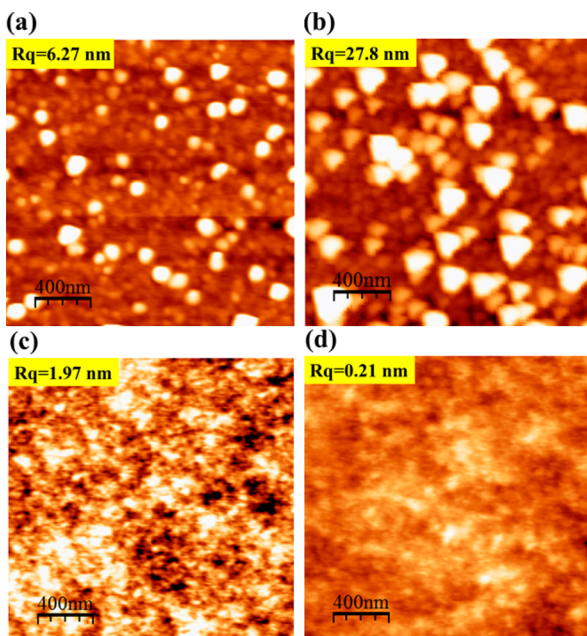


Figure 5. $2 \times 2 \mu\text{m}^2$ AFM images of the (a) Al gate electrode, (b) anodized Al_2O_3 layer, (c) spin-coated PVA on anodized Al_2O_3 , and (d) spin-coated PMMA layer on anodized $\text{Al}_2\text{O}_3/\text{PVA}$ layer.

(NMeCy2) deposited on trilayer dielectric at different T_{sub} were studied by AFM (Figure 6). The Al gate electrode after thermal deposition shows a RMS surface roughness (R_q) of 6.27 nm which after anodization gives a very rough anodized Al_2O_3 film of $R_q = 27.8$ nm. After deposition of polymer dielectric PVA, the roughness decreases up to 1.97 nm. A highly smooth and compact surface is a prerequisite for the growth of

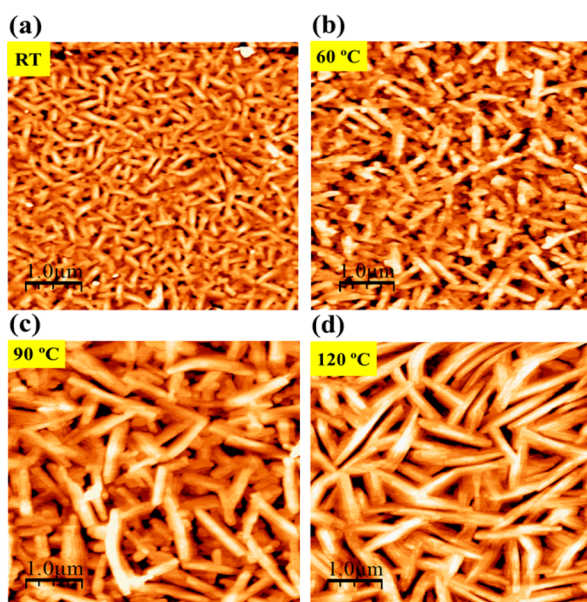


Figure 6. $5 \times 5 \mu\text{m}^2$ AFM images of NMeCy2 at T_{sub} (a) RT, (b) 60 °C, (c) 90 °C, and (d) 120 °C.

quality film, which would eventually result in efficient charge coupling between dielectric material and the channel. Finally, a flat homogeneous surface of $R_q = 0.21$ nm was obtained by covering the hydrophilic PVA dielectric layer by a very thin hydrophobic PMMA layer. The hydrophobic surface has a better interaction with organic semiconductors and passivates the scattering sites to improve the device performance. The large-scale ordered growth alignment of organic molecules over the dielectric layer helps form efficient, interconnected charge transport routes.

Figure 6 shows the AFM topography images of an organic semiconductor (NMeCy2) deposited on a trilayer dielectric system at different T_{sub} . From the AFM images of dielectric-NMeCy2 films at different T_{sub} we could deduce a fairly good microstructure/morphology-mobility correlation. Generally, with an increase in T_{sub} , the molecules gain certain thermal energy and move faster on the substrate, and the alignment would change with the diffusion rate. This led to different morphology with various T_{sub} . At RT, though the topography image showed small crystallites with compact film morphology, due to the lack of thermal activation, the charge transport is not pronounced which directly affects the carrier mobility. The AFM images of crystalline domains undergo change when T_{sub} was increased above 60 °C. At $T_{\text{sub}} = 60$ °C the dielectric-NMeCy2 surface shows crystals of around 1 μm in size in addition to the closely compacted grains with $R_q = 3.5$ nm. After increasing the T_{sub} above 60 °C, i.e., 90 and 120 °C, the continuous grains disintegrate into single elongated ones with apparently a larger number of grain gaps separating each other compared to $T_{\text{sub}} = 60$ °C which can act as charge trapping sites. The distinct morphological evolution at 90 and 120 °C may be due to the loss in viscoelasticity of the polymer dielectric films heating above its glass transition temperature. As the interface degrades the continuity of NMeCy2, the film was severely affected which resulted in alteration of crystalline packing of the molecules at the dielectric–semiconductor interface. The existence of dielectric–NMeCy2 interfacial changes in morphology at higher T_{sub} resulted in mobility degradation. The devices fabricated at $T_{\text{sub}} = 60$ °C exhibited superior field-effect behavior which is assigned to the better interconnection and tighter packing between grains that reduces the charge trapping states at the boundaries to enhance the current in the channel. On the contrary, at elevated temperature the large dendritic grains with immense voids existing in the first few NMeCy2 layers contribute to the hindrance in smooth charge transport through the OSC channel and finally reduce the carrier mobility drastically compared to the device at $T_{\text{sub}} = 60$ °C.

FESEM Analysis. Figure 7 shows FESEM images of the anodized Al_2O_3 layer, spin-coated PMMA layer on anodized $\text{Al}_2\text{O}_3/\text{PVA}$ layer, and thermally deposited NMeCy2 film on

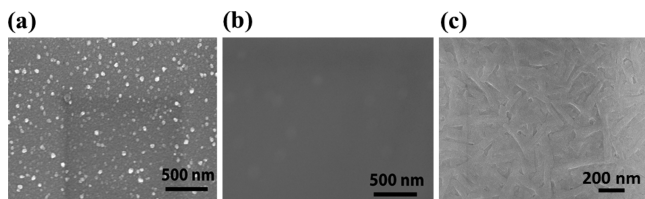


Figure 7. FESEM images of the (a) anodized Al_2O_3 layer, (b) spin-coated PMMA layer on anodized $\text{Al}_2\text{O}_3/\text{PVA}$ layer, and (c) deposited NMeCy2 layer on $\text{Al}_2\text{O}_3/\text{PVA}/\text{PMMA}$ at $T_{\text{sub}} = 60$ °C.

stack $\text{Al}_2\text{O}_3/\text{PVA}/\text{PMMA}$ at $T_{\text{sub}} = 60^\circ\text{C}$. The anodized Al_2O_3 layer displayed a rough surface with small seed-like structures. After spin coating PVA and a thin layer of PMMA on anodized Al_2O_3 , a uniform smooth film without any pores and voids was observed. A uniform and highly smooth dielectric surface is desirable for the growth of NMeCy2 semiconductor film. The FESEM image (Figure 7c) of NMeCy2 film on anodized $\text{Al}_2\text{O}_3/\text{PVA}/\text{PMMA}$ at $T_{\text{sub}} = 60^\circ\text{C}$ exhibits an interconnected network of grains which results in better device properties.

Thin-Film XRD Study. The XRD patterns of thermally deposited NMeCy2 film at $T_{\text{sub}} = 60^\circ\text{C}$ were compared with the simulated pattern obtained from single-crystal XRD data to investigate the molecular packing of NMeCy2 (Figure 8a,b).

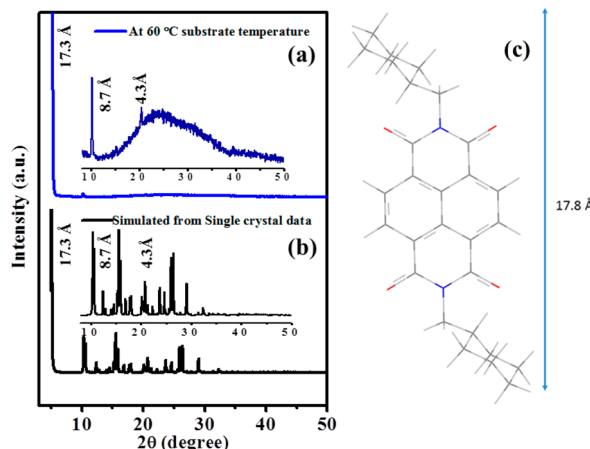


Figure 8. (a) Thermally deposited thin-film XRD pattern of NMeCy2 on a glass substrate at $T_{\text{sub}} = 60^\circ\text{C}$. (b) Simulated XRD (from single crystal) pattern of NMeCy2. (Inset: expanded area of XRD from $2\theta = 8^\circ$ to 50° .) (c) Molecular length (17.8 \AA) of NMeCy2 as calculated from DFT.

The simulated XRD pattern exhibits peaks with multiple reflections, while thin films deposited on glass substrate showed only three sharp peaks in the 5° to 50° range of 2θ . The amorphous hump at $\sim 2\theta = 25^\circ$ is due to the diffraction from the glass substrate. In both the conditions primary peaks appeared at $\sim 2\theta = 5.1^\circ$, corresponding to a d -spacing of 17.3 \AA which is close to the length of the c -axis of the NMeCy2 unit cell and is therefore attributed to (001) reflections as obtained from crystal data. The lower d_{001} value (17.3 \AA) of NMeCy2 is comparable to the molecular length of 17.8 \AA (Figure 8c) estimated from DFT,²⁶ and this difference indicates a tilted orientation of the molecule on the substrate.²⁷ The tilt angle with respect to the substrate normal is given by $\cos^{-1}(17.3/17.8) = 13.6^\circ$.²⁸ The second- and third-order diffraction peaks appear at $2\theta = 10.2^\circ$ (d -spacing = 8.7 \AA) and $2\theta = 20.4^\circ$ (d -spacing = 4.3 \AA). The d -spacing of 8.7 \AA measured from thin-film XRD confirms flip-flap stacking as observed in the case of single-crystal packing, for which the shortest distance between two identical molecules in the crystal unit is typically 8.0 \AA . In addition, the appearance of a diffraction peak at $2\theta = 20.4^\circ$ is assigned to the $\pi-\pi$ stacking and implies the existence of effective intermolecular π -orbital overlap. The match between the peak pattern obtained from the simulation of single-crystal data and the deposited thin film suggests that the growth of thin film is similar to that in bulk crystal. All the observations on morphological and structural characterization of thin films

support the better device performance of NMeCy2 at $T_{\text{sub}} = 60^\circ\text{C}$.

Transistor Properties. The OFET device fabricated at $T_{\text{sub}} = 60^\circ\text{C}$ on trilayer ($\text{Al}_2\text{O}_3/\text{PVA}/\text{PMMA}$) dielectric displayed very good linear and saturation behavior under output characteristic curves as shown in Figure 9a. The data presented

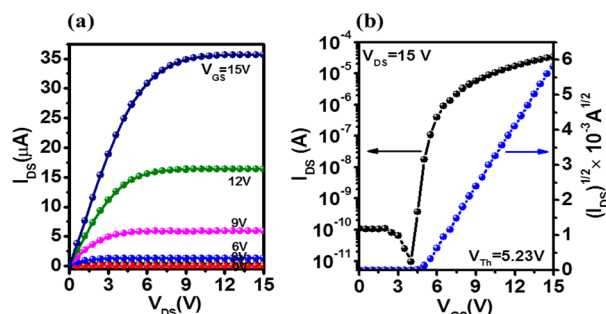


Figure 9. (a) Output and (b) transfer characteristic curves of OFET devices fabricated on $\text{Al}_2\text{O}_3/\text{PVA}/\text{PMMA}$ trilayer dielectric material.

here are the average of the ~ 10 devices in all the cases. All the devices reached the saturation region within the operating voltage 15 V . From the transfer characteristic curve (Figure 9b), the plot of $\log I_{\text{DS}}$ and square root of I_{DS} as a function of V_{GS} gives V_{Th} , μ_e , and $I_{\text{on/off}}$ to be 5.23 V , $0.6\text{ cm}^2\text{ V}^{-1}\text{ s}^{-1}$, and 10^6 , respectively. This is one of the rare low operating voltage devices with low threshold voltage and high mobility compared to the devices fabricated with similar type of molecules. The average subthreshold swing value was observed to be 0.23 V/decade , which yields an interface trap density (N_{Trap}) of $8.94 \times 10^{11}\text{ cm}^{-2}\text{ eV}^{-1}$, derived from the equation

$$N_{\text{Trap}} = \left[\frac{S \log(e)}{kT/q} - 1 \right] \frac{C_i}{q} \quad (2)$$

where S denotes subthreshold swing; k is Boltzmann's constant; T represents the absolute temperature; and C_i is 50 nF/cm^2 . The trap density at the interface with the trilayer dielectric is calculated to be near $10^{12}\text{ cm}^{-2}\text{ eV}^{-1}$ which is lower than the best values reported for OFETs.²⁹ This relatively lower N_{Trap} value for this device supports the formation of a good dielectric–NMeCy2 interface and is a very important factor to achieve high mobility. The summary of device characterization data is presented in Table 3.

CONCLUSION

In conclusion, we have demonstrated the importance of trilayer dielectrics to tune the performance of n -channel methyl cyclohexane functionalized NTCDI in the large-scale, well-organized packing in the solid state. By employing the trilayer dielectric system, we can effectively lower the operating voltage as well as V_{Th} without affecting μ_e and $I_{\text{on/off}}$ by promoting ordered growth of NMeCy2 with interconnected charge transport paths. The n -channel NMeCy2-based OFET device exhibited a saturation regime μ_e value of $0.6\text{ cm}^2\text{ V}^{-1}\text{ s}^{-1}$. We could successfully reduce the V_{Th} value up to 5.23 V and achieved high $I_{\text{on/off}}$ of 10^6 , which is one of the best performing devices among n -channel OFETs. The improved performances of the OFET device are attributed to a well-directed close intermolecular π -stacking in thin films over a large scale, the superior film forming ability of NMeCy2 at the trilayer dielectric–semiconductor interface, and reduced interfacial

Table 3. Summary of Device Characterization Data Fabricated on the Trilayer Dielectric System^a

substrate	dielectric	T _{Sub} (°C)	S (V/decade)	N _{trap} (cm ⁻² eV ⁻¹)	I _{on/off}	μ_e (cm ² /(V s))	V _{Th} (V)
glass	Al ₂ O ₃ /PVA/PMMA	60	0.23	8.94 × 10 ¹¹	10 ⁶	0.6	5.23

^aT_{Sub}: Substrate temperature, S: Subthreshold swing, N_{trap}: Interface trap density, I_{on/off}: On/off current ratio, μ_e : Electron mobility in saturation regime, V_{Th}: Threshold voltage.

defects. The phenomena occurring at the interface between the gate dielectric layer and the active channel have been marked as being closely connected to the overall device operation and performance. Our concept of trilayer dielectric with inorganic high-*k* metal-oxide and organic polymer based high-*k*/low-*k* dielectric stacked system demonstrates a significant step toward fabricating low cost, easy processed, high performance organic electronic devices.

ASSOCIATED CONTENT

Supporting Information

The detailed synthetic procedure of NMeCy2 with scanned NMRs, TGA, and DSC graphs, crystallographic data, DFT calculation for stacked dimer, and the device data at different T_{sub} are given. The Supporting Information is available free of charge on the ACS Publications website at DOI: 10.1021/acs.jpcc.5b03743.

AUTHOR INFORMATION

Corresponding Author

*E-mail: pki@iitg.ernet.in.

Notes

The authors declare no competing financial interest.

ACKNOWLEDGMENTS

The authors thank the Department of Science and Technology (DST), New Delhi, (No. DST/TSG/PT/2009/23), (No. DST/TSG/PT/2009/11), (No. DST/SERB/EMR/2014/000034), and DST-Max Planck Society, Germany (No. IGSTC MPG/PG(PKI)/2011A/48) for financial support. The Central Instruments Facility, IIT Guwahati, is acknowledged for instrumental facilities.

REFERENCES

- (1) Tang, C. W. Two Layer Organic Photovoltaic Cell. *Appl. Phys. Lett.* **1986**, *48*, 183–185.
- (2) Tang, C. W.; VanSlyke, S. A. Organic Electroluminescent Diodes. *Appl. Phys. Lett.* **1987**, *51*, 913–915.
- (3) Tsumura, A.; Koezuka, K.; Ando, T. Macromolecular Electronic Device: Field-Effect Transistor with a Polythiophene Thin Film. *Appl. Phys. Lett.* **1986**, *49*, 1210–1212.
- (4) Geyer, F. L.; Pun, A.; Hanifi, D.; Bunz, U. H. F.; Liu, Y. Growth of Reylene Diimide Crystalline Layers on Aminoalkyl Tri-ethoxysilane Monolayers for Organic Field-Effect Transistor Applications. *J. Mater. Chem. C* **2013**, *1*, 6661–6666.
- (5) Li, L.; Tang, Q.; Li, H.; Yang, X.; Hu, W.; Song, Y.; Shuai, Z.; Xu, W.; Liu, Y.; Zhu, D. An Ultra Closely π -Stacked Organic Semiconductor for High Performance Field-Effect Transistors. *Adv. Mater.* **2007**, *19*, 2613–2617.
- (6) Veres, J.; Ogier, S.; Lloyd, G. Gate Insulators in Organic Field-Effect Transistors. *Chem. Mater.* **2004**, *16*, 4543–4555.
- (7) Su, Y.; Wang, C.; Xie, W.; Xie, F.; Chen, J.; Zhao, N.; Xu, J. Low-Voltage Organic Field-Effect Transistors (OFETs) with Solution-Processed Metal-Oxide as Gate Dielectric. *ACS Appl. Mater. Interfaces* **2011**, *3*, 4662–4667.
- (8) Dao, T. T.; Matsushima, T.; Friedlein, R.; Murata, H. Controllable Threshold Voltage of a Pentacene Field-Effect Transistor based on a Double-Dielectric Structure. *Org. Electron.* **2013**, *14*, 2007–2013.
- (9) Shukla, D.; Nelson, S. F.; Freeman, D. C.; Rajeswaran, M.; Ahearn, W. G.; Meyer, D. M.; Carey, J. T. Thin Film Morphology Control in Naphthalene Diimide Based Semiconductors: High Mobility *n*-Type Semiconductor for Organic Thin Film Transistors. *Chem. Mater.* **2008**, *20*, 7486–7491.
- (10) Locklin, J.; Li, D.; Mannsfeld, S. C. B.; Borkent, E. J.; Meng, H.; Advincula, R.; Bao, Z. Organic Thin Film Transistors Based on Cyclohexyl-Substituted Organic Semiconductors. *Chem. Mater.* **2005**, *17*, 3366–3374.
- (11) Kakinuma, T.; Kojima, H.; Ashizawa, M.; Matsumoto, H.; Mori, T. Correlation of Mobility and Molecular Packing in Organic Transistors Based on Cycloalkyl Naphthalene Diimides. *J. Mater. Chem. C* **2013**, *1*, 5395–5401.
- (12) Adiga, S. P.; Shukla, D. Electronic Structure and Charge-Transport Properties of N, N'-Bis(cyclohexyl)naphthalene Diimide. *J. Phys. Chem. C* **2010**, *114*, 2751–2755.
- (13) Zhang, H.; Guo, X.; Hui, J.; Hu, S.; Xu, W.; Zhu, D. Interface Engineering of Semiconductor/Dielectric Heterojunctions toward Functional Organic Thin-Film Transistors. *Nano Lett.* **2011**, *11*, 4939–4946.
- (14) Huang, W.; Shi, W.; Han, S.; Yu, J. Hysteresis Mechanism and Control in Pentacene Organic Field-Effect Transistors with Polymer Dielectric. *AIP Adv.* **2013**, *3*, 052122.
- (15) Etten, E. A. V.; Ximenes, E. S.; Tarasconi, L. T.; Garcia, I. T. S.; Forte, M. M. C.; Boudinov, H. Insulating Characteristics of Polyvinyl Alcohol for Integrated Electronics. *Thin Solid Films* **2014**, *568*, 111–116.
- (16) Majewski, L. A.; Schroeder, R.; Grell, M. One Volt Organic Transistor. *Adv. Mater.* **2005**, *17*, 192–196.
- (17) Park, J.; Park, S. Y.; Shim, S. O.; Kang, H.; Lee, H. H. Fabrication of Sol-Gel Alumina Dielectric for Low Voltage Operating Pentacene Transistor. *Appl. Phys. Lett.* **2004**, *85*, 3283–3285.
- (18) Tsai, T. D.; Chang, J. W.; Wen, T. C.; Guo, T. F. Manipulating the Hysteresis in Poly(vinyl alcohol)-Dielectric Organic Field-Effect Transistors Toward Memory Elements. *Adv. Funct. Mater.* **2013**, *23*, 4206–4214.
- (19) Chesterfield, R. J.; McKeen, J. C.; Newman, C. R.; Frisbie, C. D.; Ewbank, P. C.; Mann, K. R.; Miller, L. L. Variable Temperature Film and Contact Resistance Measurements on Operating *n*-Channel Organic Thin Film Transistor. *J. Appl. Phys.* **2004**, *95*, 6396–6405.
- (20) Ukah, N. B.; Granstrom, J.; Gari, R. R. S.; King, G. M.; Guha, S. Low-Operating Voltage and Stable Organic Field-Effect Transistors with Poly(methyl methacrylate) Gate Dielectric Solution Deposited from a High Dipole Moment Solvent. *Appl. Phys. Lett.* **2011**, *99*, 243302.
- (21) Subbarao, N. V. V.; Gedda, M.; Iyer, P. K.; Goswami, D. K. Enhanced Environmental Stability Induced by Effective Polarization of a Polar Dielectric Layer in Tri-Layer Dielectric System of Organic Field-Effect Transistors: A Quantitative Study. *ACS Appl. Mater. Interfaces* **2015**, *7*, 1915–1924.
- (22) Spano, F. C. Excitons in Conjugated Oligomer Aggregates, Films and Crystals. *Annu. Rev. Phys. Chem.* **2006**, *57*, 217–243.
- (23) Vasimalla, S.; Senanayak, S.; Sharma, M.; Narayan, K. S.; Iyer, P. K. Improved Performance of Solution Processed *n*-Type Organic Field-Effect Transistors by Regulating the Intermolecular Interactions and Crystalline Domains on Macroscopic Scale. *Chem. Mater.* **2014**, *26*, 4030–2037.
- (24) Kolhe, N. B.; Devi, R. N.; Senanayak, S. P.; Jancy, B.; Narayan, K. S.; Asha, S. K. Structure Engineering of Naphthalene Diimides for

Improved Charge Carrier Mobility: Self Assembly by Hydrogen Bonding, Good or Bad? *J. Mater. Chem.* **2012**, *22*, 15235–15246.

(25) Shukla, D.; Welter, T. R.; Robello, D. R.; Giesen, D. J.; Lenhard, J. R.; Ahearn, W. G.; Meyer, D. M.; Rajeswaran, M. Dioxyppyrene Based Organic Semiconductors for Organic Field- Effect Transistors. *J. Phys. Chem. C* **2009**, *113*, 14482–14486.

(26) Maunoury, J. C.; Howse, J. R.; Turner, M. L. Melt Processing of Conjugated Liquids: A Simple Route to Fabricate OFETs. *Adv. Mater.* **2007**, *19*, 805–809.

(27) Gawrys, P.; Djurado, D.; Rimarcik, J.; Kornet, A.; Boudinet, D.; Jean-Marie, V.; Lukes, V.; Wielgus, I.; Zagorska, M.; Pron, A. Effect of N-Substituents on Redox, Optical and Electronic Properties of Naphthalene Bisimides Used for Field-Effect Transistors Fabrication. *J. Phys. Chem. B* **2010**, *114*, 1803–1809.

(28) Facchetti, A.; Mushrush, M.; Yoon, M. H.; Hutchison, G. R.; Ratner, M. A.; Marks, T. J. Building Blocks for *n*-Type Molecular and Polymeric Electronics. Perfluoroalkyls Versus Alkyl Functionalized Oligothiophenes (nT ; $n=2–6$). Systematics of Thin Film Microstructure, Semiconductor Performance and Modeling of Majority Charge Injection in Field-Effect Transistors. *J. Am. Chem. Soc.* **2004**, *126*, 13859–13874.

(29) McDowell, M.; Hilla, I. G. Improved Organic Thin-Film Transistor Performance using Novel Self-Assembled Monolayers. *Appl. Phys. Lett.* **2006**, *88*, 073505.